






Cite this: DOI: 10.1039/d3tc02932h

Distribution of dual additives enables efficient semi-transparent layer-by-layer architecture of organic solar cells†

Ji Youn Kim,  Sung Jae Jeon, Hyung Seok Lee, Yong Woon Han, Ye Chan Kim, Nam Gyu Yang, Gang Wook Kim,  Eun Mi Jang, Ji Hyeon Kim and Doo Kyung Moon *

Manipulating the active layer morphology to form ideal crystallinity and molecular orientation is a successful way of improving the performance of organic solar cells (OSCs). In this work, we combined the layer-by-layer (LBL) technique with dual additives introduction to precisely adjust the morphology on a PM6(FPy = 0.2):BTP-eC9 system. Importantly, 1-chloronaphthalene (CN), which has a strong dipole moment, and poly(dimethylsiloxane-co-diphenylsiloxane), dihydroxy terminated (PDMDP), which has an amorphous structure, were introduced as dual additives into the active layer. We observed that dual additives of CN and PDMDP are the keys to controlling morphology and intermolecular interaction. Consequently, the highest power conversion efficiency (PCE) of 16.51% was achieved due to the increased short-circuit current density and fill factor when dual additives under mixing and heating are introduced in a single donor layer. Furthermore, this strategy yielded high performance semi-transparent OSCs with a PCE of 11.33% and an average visible transmittance of 19.28%. The proposed strategy also demonstrated a reasonable universality with other active material systems.

Received 17th August 2023,
Accepted 4th December 2023

DOI: 10.1039/d3tc02932h

rsc.li/materials-c

Introduction

Solar cells are an indispensable energy source for the 2050 Net-Zero era and are the most infinite energy resource that has yet to be fully utilized. Types of solar cells using the photoelectric effect include Si-based solar cells, perovskite solar cells, dye-sensitized solar cells, and organic solar cells (OSCs). Among them, OSCs have attracted considerable attention due to their unique advantages such as large-area, flexibility, and transparency.^{1–3} The photoactive materials composed of a p-type organic semiconductor as donor and an n-type organic semiconductor as acceptor are considered to have critical roles in the performance of OSCs. Recently many research groups have reported high efficiency OSCs by adopting non-fullerene acceptor (NFA) Y6 derivatives as n-type acceptors.^{4,5} In general, to fabricate efficient OSCs, the donor material needs to be designed to minimize voltage loss or maximize charge carrier mobility and absorption and thus is well matched with Y6 derivatives. From this perspective, PM6, is the most widely used

as a donor material for high-performance OSCs based on Y6 derivatives. Its main chain is composed of benzodithiophene (BDT), thiophene, and benzodithiophenedione (BDD).^{6–10} Note that the BDT unit features a weak electron-donating, rigid and large coplanar structure, which has become one of the most successful building blocks in the synthesis of highly efficient donor materials. Therefore, many studies have accelerated the research on BDT-based polymer donors and demonstrated an effective strategy on highly efficient devices.^{11,12} Very recently, our group has reported a terpolymeric PM6 (FPy = 0.2) with 20% 3-fluoropyridine instead of BDD in the PM6 building block, which significantly improved its solubility in eco-friendly solvents and demonstrated its great potential for efficient and versatile OSCs.¹³ In addition, various techniques such as a ternary strategy based on BDT-derived donors have been applied to fabricate efficient devices. From these efforts, recent power conversion efficiencies (PCEs) have reached over 19%.^{14–17} However, it is still hard to produce a favorable morphology of photoactive layer for fabricating efficient OSCs. In particular, the miscibility between donor and acceptor is the most important factor.^{2,18} Other important parameters include phase separation, domain size, and crystallinity. Post-treatment processes such as thermal annealing and solvent vapor annealing (SVA) can be commonly used to include a change in the morphology of polymers, especially SVA demonstrating notable

Department of Chemical Engineering, Konkuk University, Seoul 05029, Republic of Korea. E-mail: dkmooon@konkuk.ac.kr

† Electronic supplementary information (ESI) available: Experimental details including materials, device fabrication and characterization. Images of AFM, SEM, ToF-SIMS, and GIWAXS parameters are included. See DOI: <https://doi.org/10.1039/d3tc02932h>

efficient improvement.^{19,20} Next, the introduction of solvent additives with a high boiling point compared to the solvent is considered an important process for device optimization by increasing miscibility and crystallinity. In the past decades, various solvent additives have been developed to understand the complex mechanisms in the active layer.^{21–23} Among them, it is noteworthy that the performance can be improved to uniform morphology features by introducing polymer additives, such as polydimethylsiloxane and styrene–butadiene–styrene.^{24–27} In addition, some studies reported that incorporating two different additives can reach high quality films with high performance.^{28,29} These strategies are valuable for producing efficient and stable photoactive layers.

The bulk heterojunction (BHJ) process is typically used as a processing technique for efficient OSCs due to the major advantage of forming bicontinuous interpenetrating networks of donor/acceptor composite layers. Unlike the BHJ approach, the layer-by-layer (LBL) process, thanks to the exceptional orientation and crystallinity based on Y6 derivatives, when donor and acceptor are fabricated with a p–i–n morphology, sufficient interdiffusion occurs at the interface, and a higher efficiency can be reached compared to the BHJ OSCs.^{30–33} Moreover, the LBL approach, by controlling the thickness or introducing NIR absorbing materials, not only achieves high-performance OSCs, but also semi-transparent OSCs (ST-OSCs) can be easily produced.^{34–36} Cao *et al.* reported that LBL-type devices based on a PTB7-Th/IEICO-4F system achieved high PCEs of 12% in opaque OSCs, and a balanced PCE of 8.5% and an average visible transmittance (AVT) of 21% by changing the thickness of acceptor in ST-OSCs.³⁴ Tao *et al.* reported an effective vertical component distribution strategy based on LBL-type active materials beneficial to the morphological regulation. In short, the best OSC device showed a higher PCE of 18.16% than the BHJ-type device of 16.66% by adding n-octane additive in D18-Cl donor and 1-fluoronaphthalene in Y6 acceptor, respectively.²⁹

In this study, we fabricated an efficient device using the LBL method with dual additives such as 1-chloronaphthalene (CN) and poly(dimethylsiloxane-*co*-diphenylsiloxane), dihydroxy terminated (PDMDP) that affect the morphology formation of PM6(FPy = 0.2), which was reported in previous our work.¹³ Both additives were introduced into the PM6(FPy = 0.2) layer and the acceptor layer was then coated on the top to form the LBL-processed p–i–n morphology. Specifically, we examined the changes in the photoactive layer with and without heat treatment after mixing two additives separately. This technique of dual additives that benefited from heating and mixing treatments could provide synergistic effects in short-circuit current density (J_{sc}) and fill factor (FF) due to the fine-tuned morphology. A comparison of the performance of active layers with respect to the additive and coating method showed the influence of electrostatic potential (ESP) results on intermolecular interactions, which demonstrated an efficient charge transfer effect of devices formed by the LBL process and dual additives. As a result, from the dual additives and LBL process effects, the optimized device leads to the best performance with

a PCE of 16.51%. The proposed strategy was further applied for fabricating efficient ST-OSCs. Note that all LBL films enhanced the AVT in the region of 320 to 780 nm compared to that of BHJ films. The best performing ST-OSC device yielded a PCE of 11.33% with an AVT of 19.28%. Finally, the proposed strategy showed a reasonable universality through different active materials.

Results and discussion

Fig. 1(a) depicts the molecular structures of photoactive materials (donor and acceptor, PM6(FPy = 0.2) and BTP-eC9) and additives (CN and PDMDP). To understand the interactions between each additive and photoactive materials, we calculated ESP distributions of each material *via* density functional theory (DFT) using the B3LYP functional and 6-31G(d) basis sets. As shown in Fig. 1(b), both CN and PDMDP additives as well as the PM6(FPy = 0.2) donor show negative surfaces upon their main conjugated backbones, while most of the surface of the BTP-eC9 acceptor is positive. This indicates that both additives can form strong intermolecular interactions with BTP-eC9. In particular, PDMDP exhibits a more negatively charged surface and can be expected to have stronger intermolecular interaction with the acceptor compared to the donor. These results imply that the effects of charge generation and separation of the active materials could be sensitively changed according to the additive combination.^{37–39}

Fig. 1(c) depicts a schematic diagram of the conventional structure (ITO/PEDOT:PSS/Active layer/PDINN/Ag). In detail, the active layer can be processed by BHJ and LBL structures with PM6(FPy = 0.2) and BTP-eC9, respectively. The four additive combinations of CN, PDMDP, CN + PDMDP, and (H) CN + PDMDP were systematically introduced *via* BHJ and LBL methods and named as device 1, device 2, device 3, and device 4.

Note that device 4 is processed after a dual additives heating process to improve the homogeneity of solutions.⁴⁰

Fig. 2 and Table 1 show the J - V and EQE curves of the optimized OSC devices. Table S1 (ESI[†]) shows all LBL-processed devices with conditions of (H) CN + PDMDP with various ratios

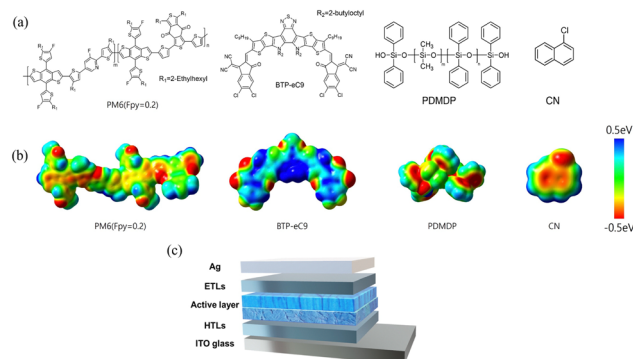


Fig. 1 Materials and devices characterization: (a) chemical molecular structures of active materials (PM6(FPy = 0.2) and BTP-eC9) and additives (CN and PDMDP). (b) ESP distribution with the dipole moment of CN and PDMDP. (c) Device architecture of LBL-processed OSCs.

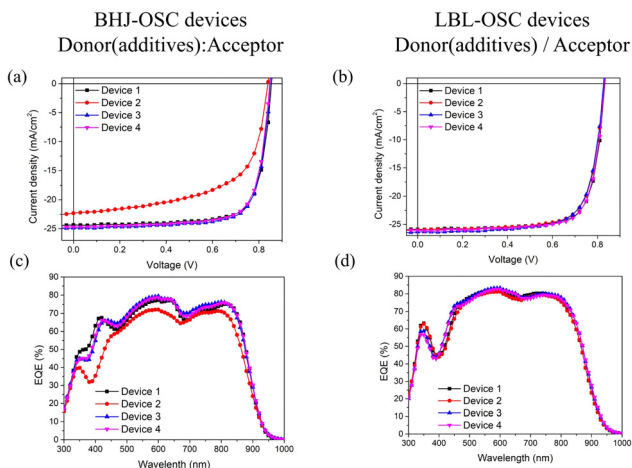


Fig. 2 (a) and (b) J - V and (c) and (d) EQE curves of the optimized OSC devices based on (a) and (c) BHJ and (b) and (d) LBL processes with respect to the additive: CN (device 1), PDMDP (device 2), CN + PDMDP (device 3), and (H) CN + PDMDP (device 4).

of CN and PDMDP. For single additive CN, compared with device 1-BHJ, the PCE of device 1-LBL was enhanced from 15.26% to 16.41%. When introducing PDMDP, the device 2-BHJ showed a relatively low PCE of 11.48% whereas device 2-LBL exhibited a reasonable PCE of 16.04%. This result of device 2-BHJ might be due to the relatively unfavorable morphology derived from excessive intermolecular interactions between BTP-eC9 and PDMDP, which is consistent with the results of ESP analysis. After introducing dual additives with CN + PDMDP, the PCEs of device 3-BHJ and device 3-LBL were increased to 15.78% and 16.06%, respectively, compared to those of device 2-BHJ and device 3-LBL. Surprisingly, this improved performance of device 3-BHJ might be due to the preferential and stably formed dipole-dipole interaction ($\text{Cl} \cdots \text{OH}$) between the Cl atom of CN and OH terminated groups of PDMDP.^{67–69} Lastly, device 4-BHJ and device 4-LBL with dual additives which have an additional annealing process ((H) CN + PDMDP), achieved PCEs of 15.74% and 16.51%, respectively. Notably, the highest performance was achieved in device 4-LBL, which is attributed to the relatively improved FF value compared to that of device 3-LBL. Fig. 2(c) and (d) present the EQE spectra of BHJ and LBL devices with respect to the additive, respectively. Compared with both graphs, the photo-response of LBL devices is higher than that of BHJ devices in

the wavelength range of 700–900 nm. As shown in Fig. 2 and Table 1, the main parameter contributing to the enhanced PCEs is J_{sc} . The results show the dual additives strategy can be controlled *via* the LBL technique based on an understanding of molecular interactions.

Fig. 3 and Fig. S1 (ESI[†]) show the UV-Vis absorption spectra of neat PM6(FPy = 0.2), BTP-eC9, and LBL films according to the additives. For all neat PM6(FPy = 0.2) films, two absorption peaks, A_{0-0} and A_{0-1} at near 575 and 625 nm were observed, which are closely related with the molecular aggregation.^{40,43} Therefore, the proposed additives have no effect on the intra/inter-molecular transitions of PM6(FPy = 0.2). Nevertheless, with the introduction of dual additives, the absorption spectra of film 3 and film 4 showed relative increments of A_{0-0}/A_{0-1} intensity ratio and slightly red-shifted waveforms, which is beneficial to enhance the molecular crystallinity and photon absorption.^{41,42} Notably, this trend was similarly exhibited in the case of dual additives/acceptor films as shown in Fig. S1(a) (ESI[†]). More importantly, the absorption spectra of LBL-processed films with different additive conditions are consistent with the photo-response properties for the corresponding EQE curves as mentioned above. These results thus explain the significant relationship between UV-Vis data and photovoltaic performance. Specifically, the best performance of device 4-LBL might be related to the unique morphology derived from dual additives which were incorporated into donor/acceptor to form aggregates appropriately. As shown in Fig. S1(b) (ESI[†]), we further investigated the neat BTP-eC9 films containing the additives, which also shows that dual additives can manipulate the molecular aggregate behavior positively. This is likely to be part of the reason why low PCEs are yielded in BHJ devices. In other words, it might be caused by strong intermolecular interactions between additives and acceptor that induce the disordered or oversized aggregation in BHJ films.^{24,44,45} Comprehensively, LBL films have better molecular orientation and morphology modification, which can meet the requirements of efficient devices.^{46–48}

To understand the morphological characteristics of single donor and active layers, atomic force microscopy (AFM) and scanning electron microscopy (SEM) were carried out. Fig. 4(a) and Fig. S2(a) (ESI[†]) show the AFM images of neat polymer and LBL-processed blend films, respectively. As shown in Fig. S2(a) (ESI[†]), the root-mean-square (RMS) values of device 1, 2, 3, and 4 in neat polymer films were measured to be 0.836 nm,

Table 1 Photovoltaic parameters of the optimized OSC devices under AM 1.5 G illumination, 100 mW cm⁻²

	Structure	J_{sc} [mA cm ⁻²]	V_{oc} [V]	FF [%]	PCE ^a [%]
Device 1 CN	BHJ	23.43 (23.30 ± 0.23)	0.853 (0.851 ± 0.002)	76.38 (76.35 ± 0.03)	15.26 (15.13 ± 0.12)
	LBL	25.91 (25.73 ± 0.17)	0.832 (0.831 ± 0.001)	76.08 (76.00 ± 0.07)	16.41 (16.25 ± 0.13)
Device 2 PDMDP	BHJ	22.41 (22.10 ± 0.26)	0.839 (0.833 ± 0.005)	61.03 (60.80 ± 0.20)	11.48 (11.23 ± 0.24)
	LBL	26.01 (25.83 ± 0.15)	0.827 (0.822 ± 0.004)	74.56 (74.36 ± 0.18)	16.04 (15.88 ± 0.15)
Device 3 CN + PDMDP	BHJ	24.53 (24.31 ± 0.20)	0.847 (0.845 ± 0.002)	75.94 (75.85 ± 0.09)	15.78 (15.66 ± 0.11)
	LBL	26.35 (26.01 ± 0.23)	0.827 (0.823 ± 0.003)	73.74 (73.64 ± 0.09)	16.06 (15.97 ± 0.08)
Device 4 (H) CN + PDMDP	BHJ	24.44 (24.20 ± 0.18)	0.845 (0.840 ± 0.003)	76.19 (76.17 ± 0.02)	15.74 (15.60 ± 0.13)
	LBL	26.07 (25.98 ± 0.15)	0.831 (0.829 ± 0.002)	76.24 (76.19 ± 0.04)	16.51 (16.30 ± 0.21)

^a Champion value and average values (in parenthesis) are obtained from 10 devices.

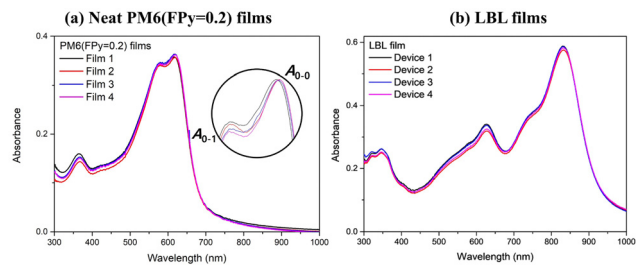


Fig. 3 UV-Vis absorption spectra of (a) neat PM6(FPy = 0.2) and (b) LBL-processed blend films with respect to the additive. The inset in Fig. 3(a) shows the zoomed and normalized UV-Vis absorption spectra.

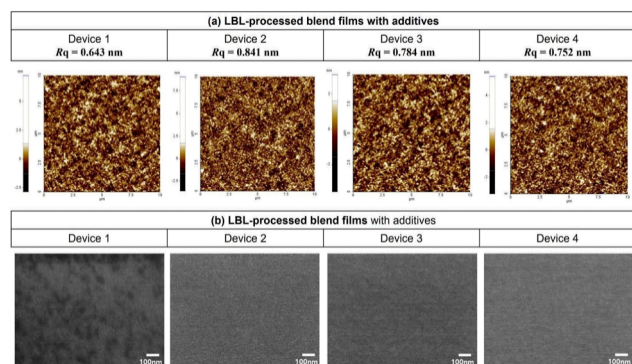


Fig. 4 (a) AFM height and (b) SEM images of LBL-processed blend films with respect to the additive.

1.019 nm, 0.864 nm, and 0.857 nm, respectively.^{1,26,49–52} Although the PDMDP-based films showed relatively high RMS values compared to the CN-based film, device 4 with dual additives and an additional annealing process presents a smaller roughness and forms a smoother surface. This means that well-mixed additives contributed a fine-tuned morphology in the donor layer.^{53,54} These results were also observed in AFM images for LBL-processed blend films. The dual additives in LBL films led to optimal phase formation and separation between donor and acceptor, which can contribute to the increment of J_{SC} and FF. Fig. 4(b) and Fig. S2(b) (ESI[†]) show SEM images of neat polymer and LBL-processed blend films with respect to the additive. For device 1 with CN additive, both neat polymer and LBL films exhibit large grain boundaries with dark dots, which might be derived from the strong aggregated donor and/or acceptors. In contrast, all PDMDP-based films have relatively smooth surfaces. Among them, when introducing dual additives with heat treatment, the surface with the oversized aggregation could be reduced, which can be aided with control of charge transport pathways.

For better understanding the additives effect on the morphology of LBL-processed active layers, we further conducted time-of-flight secondary spectrometry (ToF-SIMS) measurements, which quantitatively monitor the vertical profiles of each component across the whole thickness of active layers (Fig. 5(a) and Fig. S3, ESI[†]).^{55,56} All samples were prepared on ITO substrate with the same conditions as the optimized

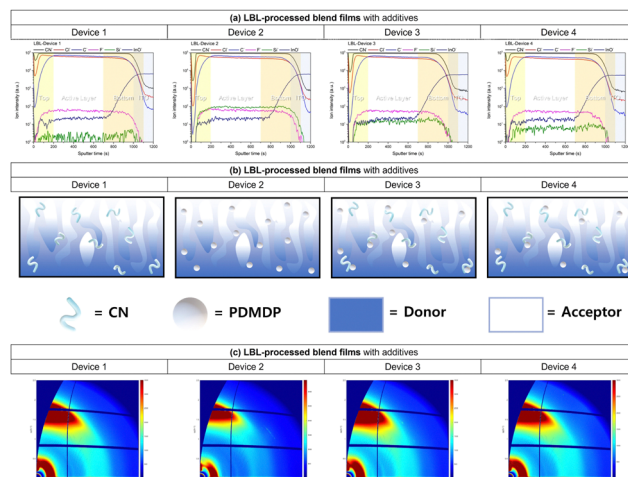


Fig. 5 (a) ToF-SIMS depth profiles of LBL-processed blend films coated on ITO glass with respect to the additive: Tracking the ion intensity of CN⁻ (BTP-eC9), Cl⁻ (BTP-eC9), C⁻ (both PM6(FPy = 0.2) and BTP-eC9)), F⁻ (PM6(FPy = 0.2), Si⁻ (PDMDP), and InO⁻ (ITO)) groups. (b) Schematic illustration of the corresponding LBL-processed blend films obtained from the ToF-SIMS results. (c) GIWAXS patterns of the corresponding LBL-processed blend films.

devices. Note that CN⁻ (BTP-eC9), Cl⁻ (BTP-eC9), C⁻ (both PM6(FPy = 0.2) and BTP-eC9), F⁻ (PM6(FPy = 0.2), Si⁻ (PDMDP), and InO⁻ (ITO)) groups were detected. From the top to the bottom of all samples in the active layer, all ion groups except for the Si⁻ group were observed, implying BTP-eC9 and PM6(FPy = 0.2) were both distributed throughout the entire active layer enabling efficient charge transfer. When PDMDP was introduced as a single additive into active layers, the device 2-BHJ showed a poor PCE of 11.48% whereas the device 2-LBL exhibited a reasonable PCE over 16%, indicating that PDMDP can aid in controlling the morphology of the donor layer. Interestingly, device 4-LBL with dual additives yielded the highest performance of 16.51% despite PDMDP molecules being distributed on the whole region of the active layer according to the result of ToF-SIMS. This result might be due to the fine-tuned morphology derived from preferentially formed intermolecular hydrogen bonds between the OH terminal groups of PDMDP and F groups of the polymer donor. Interdiffusion between donor and acceptor with respect to the additive was formed over the entire range in LBL films.^{29,57} Note the molecular orientation of the corresponding LBL films, as shown in Fig. 5(b).

To explore the molecular packing behaviors in neat polymer donor and LBL-processed blend films with respect to the additive, grazing-incidence wide-angle X-ray scattering (GIWAXS) measurements were employed (Fig. 5(c) and Fig. S4(a), ESI[†]). The corresponding line-cut profiles in the out-of-plane (OOP) and in-plane (IP) directions are presented in Fig. S4(b) (ESI[†]). Detailed parameters from GIWAXS profiles of all films in the OOP are summarized in Tables S2 and S3 (ESI[†]). All neat polymer films exhibit bimodal structures mixed with both face-on ((010)) and edge-on orientations ((100) and (300)).^{33,58,59} It is noted that CN additive can contribute to the enhanced

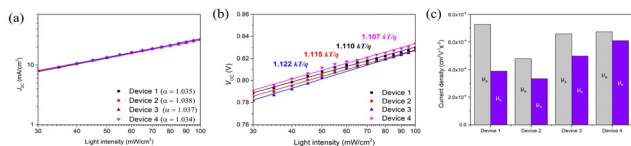


Fig. 6 (a) Light intensity dependence of J_{SC} and (b) V_{OC} of the optimized OSC devices based on the LBL process. (c) Hole and electron-only mobilities of the corresponding OSC devices.

crystallinity in (300) whereas PDMDP additive can increase the crystalline structures in both (100) and (010). With synergistic effects of CN and PDMDP, the neat polymer film with (H) CN + PDMDP showed the balanced crystalline structures in (100), (300), and (010), resulting in the shortest d -spacings in all the corresponding planes. After introducing BTP-eC9, all LBL blend films exhibited an improved π - π stacking effect at near $q = 1.75 \text{ \AA}^{-1}$ in the OOP and new lamellar peak at near $q = 0.37 \text{ \AA}^{-1}$ in the IP. These results indicate that all LBL films achieved the balanced miscibility and crystallinity. In short, the LBL film with CN showed the highest crystal coherence length

(CCL) value in (100) whereas the LBL film with CN + PDMDP has the smallest CCL₍₁₀₀₎ value, which can be correlated to the FF values of the corresponding OSC devices. Although LBL films with dual additives have relatively low CCL₍₁₀₀₎, as the CCL₍₀₁₀₎ values are gradually increased, the device 4 achieved the highest CCL₍₀₁₀₎ of 24.44 Å and the shortest π - π stacking distance of 3.56 Å, which resulted in the highest PCE. This result means the dual additives and LBL strategy increased the crystallinity along their intermolecular interaction and assisted molecular orientation and specified their aggregation.^{60,61}

Fig. 6 and Table S4 (ESI[†]) show the measurement results of the charge mechanism and carrier dynamics of the optimized OSC devices based on the LBL process with respect to the additive. Fig. 6(a) and (b) show the dependence of J_{SC} and V_{OC} on the light intensity (P_{Light}) from 0.3 to 1 sun. Fig. 6(a) presents the J_{SC} vs. P_{Light} curve using the power-law exponent between J_{SC} and P_{Light} , $J_{SC} \propto (P_{Light})^\alpha$, showing that the α values of all devices converge to 1.034 closely. If the α value is close to 1, it could be suggested that bimolecular recombination is suppressed efficiently.^{62,63} Meanwhile, Fig. 6(b) shows the V_{OC} -

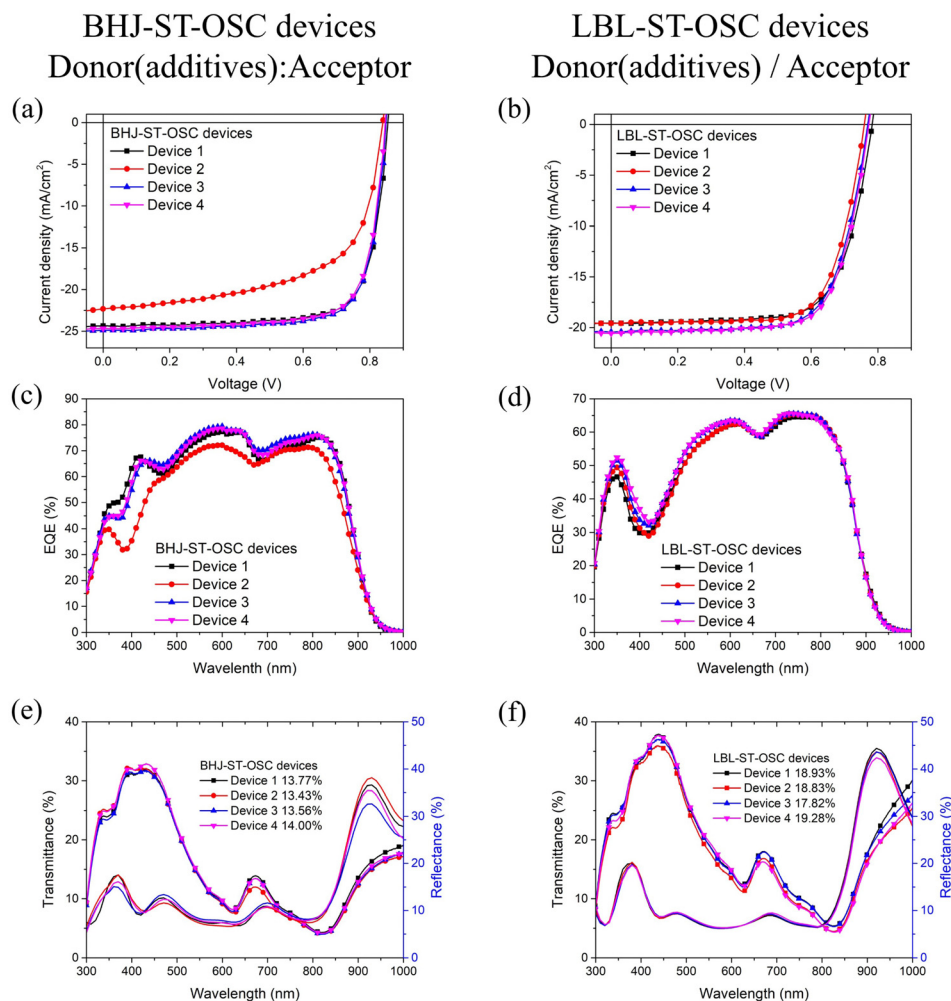


Fig. 7 (a) and (b) J - V and (c) and (d) EQE curves of the optimized ST-OSC devices based on (a), (c), and (e) BHJ and (b), (d), and (f) LBL processes with respect to the additive. (e) and (f) The transmission and reflection spectra of the corresponding ST-OSC devices.

Table 2 Photovoltaic parameters of the optimized ST-OSC devices under AM 1.5 G illumination, 100 mW cm⁻²

	Structure	J_{SC} [mA cm ⁻²]	V_{OC} [V]	FF [%]	PCE ^a [%]	AVT [%]
Device 1 CN	BHJ	18.10 (17.90 ± 0.18)	0.780 (0.778 ± 0.002)	66.68 (66.62 ± 0.06)	9.41 (9.30 ± 0.11)	13.77
	LBL	19.55 (19.40 ± 0.13)	0.783 (0.781 ± 0.002)	70.90 (70.80 ± 0.10)	10.85 (10.55 ± 0.30)	18.93
Device 2 PDMDP	BHJ	16.11 (15.85 ± 0.25)	0.814 (0.810 ± 0.004)	59.61 (59.40 ± 0.20)	7.81 (7.40 ± 0.38)	13.43
	LBL	19.58 (19.35 ± 0.22)	0.759 (0.753 ± 0.006)	72.06 (71.91 ± 0.15)	10.71 (10.50 ± 0.21)	17.82
Device 3 CN + PDMDP	BHJ	18.31 (18.19 ± 0.12)	0.801 (0.798 ± 0.003)	70.25 (70.16 ± 0.09)	10.30 (10.15 ± 0.15)	13.56
	LBL	20.42 (20.25 ± 0.26)	0.769 (0.767 ± 0.002)	70.91 (70.80 ± 0.10)	11.14 (11.02 ± 0.12)	18.83
Device 4 (H) CN + PDMDP	BHJ	18.13 (17.98 ± 0.11)	0.811 (0.809 ± 0.002)	70.72 (70.65 ± 0.07)	10.40 (10.25 ± 0.13)	14.00
	LBL	20.57 (20.30 ± 0.26)	0.773 (0.770 ± 0.003)	71.27 (71.22 ± 0.05)	11.33 (11.23 ± 0.08)	19.28

^a Champion value and average values (in parenthesis) are obtained from 10 devices.

$\ln(P_{\text{Light}})$ plot, in which device 4 has the lowest value of 1.107 kT q⁻¹, which is close to 1. Therefore, dual additives with an additional annealing process could decrease trap-assisted recombination and achieve a high FF.⁶⁴ Fig. 6(c) and Table S2 (ESI[†]) show the calculated carrier mobilities of hole and electron-only devices of the corresponding OSC devices measured using the space charge limited current (SCLC) method. The hole mobility (μ_h) of device 1, 2, 3, and 4 is 3.89×10^{-4} , 3.34×10^{-4} , 4.99×10^{-4} , and 6.09×10^{-4} cm² V⁻¹ s⁻², respectively. The electron mobility (μ_e) of device 1, 2, 3, and 4 is 7.28×10^{-4} , 4.81×10^{-4} , 6.59×10^{-4} , and 6.74×10^{-4} cm² V⁻¹ s⁻², respectively. In particular, the μ_e and μ_h ratio of device 4 was the most balanced.¹² These results indicate that the dual additives and LBL strategy provides better charge transport and the low recombination led to the high J_{SC} and FF.^{27,29,56}

Based on the above-mentioned results of high-performance OSCs with dual additives and the LBL technique, it is highly desirable to explore the photovoltaic properties of the ST-OSC devices to obtain further meaningful achievements. Fig. 7(a–d) show J - V curves of the optimized ST-OSC devices. Fig. 7(e) and (f) show the transmittance and reflection characteristics of the corresponding ST-OSC devices. The photovoltaic parameters with AVT values are summarized in Table 2. Overall, AVT and PCE in LBL-ST-OSCs showed substantial improvements compared to that of BHJ-ST-OSCs. Briefly, with the synergistic effects of dual additives and the LBL technique, the LBL-ST-OSC device 4 showed the best PCE of 11.33%, which is higher by approximately 1% than that of BHJ ST-OSC (10.40%). This is attributed to the enhanced EQE response in the range of 700–900 nm, which is the same as the result of the corresponding opaque device. This result can also be observed in the transmittance and reflection response in the same range. Remarkably, LBL-ST-OSC device 4 exhibited the highest AVT of 19.28% due to the enhanced transmittance in the range of 400–700 nm which is the absorption region of the polymer donor. In contrast, the BHJ-ST-OSC device 4 has the relatively low AVT of 14.0%. The EQE + T + R curves of all ST-OSC devices are shown in Fig. S5 (ESI[†]). All ST-OSC devices exhibited reliability between efficiency and transmittance.

Lastly, to demonstrate the universality of the dual additives and LBL strategy, the photovoltaic properties of BHJ and LBL-OSC devices based on various active materials (PM6 and L8-BO; D18 and BTP-eC9) were investigated with CN, CN + PDMDP. Noted for all OSC devices. The photovoltaic parameters are

summarized in Table S5 (ESI[†]). The photovoltaic results can be compared with each other as shown in Fig. S6 (ESI[†]). For all active material systems, devices with dual additives show better or more reasonable performance than devices with CN. Briefly, for both PM6 and D18-based active materials, the best PCEs of 16.65% and 16.59% were achieved in BHJ and LBL-OSC devices with CN + PDMDP, respectively. Recent studies showed that the LBL strategy and dual additives strategy both have great potential for fabricating efficient and transparent ST-OSC devices.^{34,36,65,66} In this work, our results indicate that combining these two strategies can exert a synergistic effect and provide even more improved device performance by manipulating the active layer morphology.

Conclusions

Dual additives and the LBL technique were introduced as a strategy for fabricating efficient high-performance devices. In summary, LBL-processed active layers showed a remarkable performance compared with BHJ-processed active layers, which provides further insight into the role of the dual additive based on the molecular interaction between donor and acceptor. The dual additives of CN and PDMDP with thermal annealing provided synergistic effects on both the J_{SC} and FF of the LBL-processed device due to the fine-tuned morphology. As a result, the highest PCE of 16.51% was achieved among the opaque OSC devices. Note that all LBL films enhanced AVT values with an amount of approximately 5% in the region of 320 to 780 nm compared to that of BHJ films. Therefore, ST-OSC devices were further fabricated, and the best device yielded the balanced PCE of 11.33% and AVT of 19.28%. This strategy demonstrated a good universality for fabricating devices, and can be applied to the other active material systems such as PM6:L8-BO and D18/BTP-eC9.

Author contributions

All authors have discussed the results and participated in the writing of this manuscript. All ideas, experimental data, most data collection/analysis, and preparation of manuscript by J. Y. K. contributed to interpreting the data and preparation of the manuscript based on the obtained results and writing and editing. S. J. J. contributed to the synthesis of materials,

preparation of the manuscript based on the obtained results and Writing – review & editing. H. S. L contributed to interpreting the data and preparation of manuscript based on the obtained results and writing and editing. Y. W. H contributed to the preparation of the manuscript based on the obtained results. Y. C. K. N. G. Y. G. W. K and E. M. J. contributed to preparation of the manuscript based on the obtained results and Writing – review & editing. J. H. K. contributed to the preparation of manuscript based on the obtained results and Writing – review & editing. D. K. M conceptualization, reviewed, edited, made overall correction, and directed the project.

Conflicts of interest

There are no conflicts to declare.

Acknowledgements

This paper was supported by Konkuk University in 2020.

References

- X. Xu, L. Yu, H. Yan, R. Li and Q. Peng, *Energy Environ. Sci.*, 2020, **13**, 4381–4388.
- Y. W. Han, S. J. Jeon, H. S. Lee, H. Park, K. S. Kim, H. Lee and D. K. Moon, *Adv. Energy Mater.*, 2019, **9**, 1902065.
- S. J. Jeon, Y. W. Han and D. K. Moon, *Small*, 2019, **15**, 1902598.
- J. Yuan, Y. Zhang, L. Zhou, G. Zhang, H. L. Yip, T. K. Lau, X. Lu, C. Zhu, H. Peng, P. A. Johnson, M. Leclerc, Y. Cao, J. Ulanski, Y. Li and Y. Zou, *Joule*, 2019, **3**, 1140–1151.
- Y. Cui, H. Yao, J. Zhang, K. Xian, T. Zhang, L. Hong, Y. Wang, Y. Xu, K. Ma, C. An, C. He, Z. Wei, F. Gao and J. Hou, *Adv. Mater.*, 2020, **32**, 1908205.
- M. Zhang, X. Guo, W. Ma, H. Ade and J. Hou, *Adv. Mater.*, 2015, **27**, 4655–4660.
- M. Zhang, X. Guo, S. Zhang and J. Hou, *Adv. Mater.*, 2014, **26**, 1118–1123.
- R. Yu, G. Wu and Z. Tan, *J. Energy Chem.*, 2021, **61**, 29–46.
- S. Zhang, Y. Qin, J. Zhu and J. Hou, *Adv. Mater.*, 2018, **30**, 1800868.
- Z. He, C. Zhong, S. Su, M. Xu, H. Wu and Y. Cao, *Nat. Photonics*, 2012, **6**, 591–595.
- M. Zhang, X. Xu, L. Yu and Q. Peng, *J. Power Sources*, 2021, **499**, 229961.
- J. S. Park, G. Kim, D. Lee, S. Lee, B. Ma, S. Cho and B. J. Kim, *Adv. Funct. Mater.*, 2020, **30**, 2005787.
- S. J. Jeon, N. G. Yang, J. Y. Kim, Y. C. Kim, H. S. Lee and D. K. Moon, *Small*, 2023, **19**, 2301803.
- Y. Cui, Y. Xu, H. Yao, P. Bi, L. Hong, J. Zhang, Y. Zu, T. Zhang, J. Qin, J. Ren, Z. Chen, C. He, X. Hao, Z. Wei and J. Hou, *Adv. Mater.*, 2021, **33**, 2102420.
- C. He, Y. Pan, Y. Ouyang, Q. Shen, Y. Gao, K. Yan, J. Fang, Y. Chen, C.-Q. Ma, J. Min, C. Zhang, L. Zuo and H. Chen, *Energy Environ. Sci.*, 2022, **15**, 2537–2544.
- L. Zhu, M. Zhang, J. Xu, C. Li, J. Yan, G. Zhou, W. Zhong, T. Hao, J. Song, X. Xue, Z. Zhou, R. Zeng, H. Zhu, C. C. Chen, R. C. I. MacKenzie, Y. Zou, J. Nelson, Y. Zhang, Y. Sun and F. Liu, *Nat. Mater.*, 2022, **21**, 656–663.
- J. Qin, L. Zhang, C. Zuo, Z. Xiao, Y. Yuan, S. Yang, F. Hao, M. Cheng, K. Sun, Q. Bao, Z. Bin, Z. Jin and L. Ding, *J. Semicond.*, 2021, **42**, 010501.
- H. Zhang, Y. Li, X. Zhang, Y. Zhang and H. Zhou, *Mater. Chem. Front.*, 2020, **4**, 2863–2880.
- Z. Wang, Z. Peng, Z. Xiao, D. Seyitliyev, K. Gundogdu, L. Ding and H. Ade, *Adv. Mater.*, 2020, **32**, 2005386.
- V. Piradi, X. Xu, Z. Wang, J. Ali, Q. Peng, F. Liu and X. Zhu, *ACS Appl. Mater. Interfaces*, 2019, **11**, 6283–6291.
- S. Chen, S. Jung, H. J. Cho, N. H. Kim, S. Jung, J. Xu, J. Oh, Y. Cho, H. Kim, B. Lee, Y. An, C. Zhang, M. Xiao, H. Ki, Z. G. Zhang, J. Y. Kim, Y. Li, H. Park and C. Yang, *Angew. Chem., Int. Ed.*, 2018, **57**, 13277–13282.
- H. Zeng, C. Hu, D. Wu and J. Xia, *ChemPlusChem*, 2022, **87**, e202200045.
- C. Jiang, M. Zhao, X. Chen, X. Li and H. Wang, *Dyes Pigm.*, 2020, **174**, 108044.
- H. Fu, W. Gao, Y. Li, F. Lin, X. Wu, J. H. Son, J. Luo, H. Y. Woo, Z. Zhu and A. K.-Y. Jen, *Small Methods*, 2020, **4**, 2000687.
- T. Kumari, M. Moon, S.-H. Kang and C. Yang, *Nano Energy*, 2016, **24**, 56–62.
- S. Chen, C. He, Y. Li, T. Chen, X. Xia, W. Fu, M. Shi, X. Lu, L. Zuo and H. Chen, *J. Mater. Chem. C*, 2022, **10**, 2749–2756.
- C. Jiang, H. Li, S. Yang, X. Li and H. Wang, *ChemistrySelect*, 2021, **6**, 1852–1861.
- J. Y. Choi, Y. W. Han, S. J. Jeon, E. J. Ko and D. K. Moon, *Sol. Energy*, 2019, **185**, 1–12.
- X. Li, R. Zhu, Z. He, X. Du, H. Lin, C. Zheng, G. Yang, Z. Chen and S. Tao, *ACS Appl. Mater. Interfaces*, 2022, **14**, 25842–25850.
- H. Tang, Y. Li, H. Liu, J. Wu, L. Chen, Y. Fu and Z. Xie, *J. Mater. Chem. C*, 2022, **10**, 3720–3728.
- M. Ren, G. Zhang, Z. Chen, J. Xiao, X. Jiao, Y. Zou, H. L. Yip and Y. Cao, *ACS Appl. Mater. Interfaces*, 2020, **12**, 13077–13086.
- Q. He, W. Sheng, M. Zhang, G. Xu, P. Zhu, H. Zhang, Z. Yao, F. Gao, F. Liu, X. Liao and Y. Chen, *Adv. Energy Mater.*, 2021, **11**, 2003390.
- R. Yu, G. Wu, Y. Cui, X. Wei, L. Hong, T. Zhang, C. Zou, S. Hu, J. Hou and Z. Tan, *Small*, 2021, **17**, 2103497.
- Y. Song, K. Zhang, S. Dong, R. Xia, F. Huang and Y. Cao, *ACS Appl. Mater. Interfaces*, 2020, **12**, 18473–18481.
- H. Wang, P. Cheng, S. Tan, C. Chen, B. Chang, C. Tsao, L. Chen, C. Hsieh, Y. Lin, H. Cheng, Y. Yang and K. Wei, *Adv. Energy Mater.*, 2021, **11**, 2003576.
- C. Xu, K. Jin, Z. Xiao, Z. Zhao, Y. Yan, X. Zhu, X. Li, Z. Zhou, S. Y. Jeong, L. Ding, H. Y. Woo, G. Yuan and F. Zhang, *Sol. RRL*, 2022, **6**, 2200308.
- X. Wang, S. Li, L. Zhao, C. Xu and J. Gao, *Chin. J. Chem. Eng.*, 2020, **28**, 532–540.
- X. Liao, Y. Cui, X. Shi, Z. Yao, H. Zhao, Y. An, P. Zhu, Y. Guo, X. Fei, L. Zuo, K. Gao, F. Lin, Q. Xie, L. Chen, W. Ma, Y. Chen and A. K. Y. Jen, *Mater. Chem. Front.*, 2020, **4**, 1507–1518.

- 39 H. Bai, Q. An, M. Jiang, H. S. Ryu, J. Yang, X. Zhou, H. Zhi, C. Yang, X. Li, H. Y. Woo and J. Wang, *Adv. Funct. Mater.*, 2022, **32**, 2200807.
- 40 S. Morariu, C. E. Brunchi, M. Cazacu and M. Bercea, *J. Chem. Eng. Data*, 2011, **56**, 1468–1475.
- 41 C. Jiang, M. Zhao, X. Chen, X. Li and H. Wang, *Dyes Pigm.*, 2020, **174**, 108044.
- 42 H. Liu, Y. Fu, Z. Chen, J. Wang, J. Fu, Y. Li, G. Cai, C. Su, U. Jeng, H. Zhu, G. Li and X. Lu, *Adv. Funct. Mater.*, 2023, **33**, 2303307.
- 43 N. Yang, Y. Cheng, S. Kim, B. Huang, Z. Liu, J. Deng, J. Wang, C. Yang, F. Wu and L. Chen, *ChemSusChem*, 2022, **15**, e202200138.
- 44 F. Dou, J. Li, H. Men and X. Zhang, *Polymers*, 2020, **12**(4), 786.
- 45 J. S. Kim, Z. Fei, S. Wood, D. T. James, M. Sim, K. Cho, M. J. Heeney and J. S. Kim, *Adv. Energy Mater.*, 2014, **4**, 1400527.
- 46 G. Jo, J. Jung and M. Chang, *Polymers*, 2019, **11**(2), 332.
- 47 M. Chang, J. Lee, N. Kleinhenz, B. Fu and E. Reichmanis, *Adv. Funct. Mater.*, 2014, **24**, 4457–4465.
- 48 J. Wu, G. Li, J. Fang, X. Guo, L. Zhu, B. Guo, Y. Wang, G. Zhang, L. Arunagiri, F. Liu, H. Yan, M. Zhang and Y. Li, *Nat. Commun.*, 2020, **11**, 4612.
- 49 R. Ma, T. Liu, Z. Luo, Q. Guo, Y. Xiao, Y. Chen, X. Li, S. Luo, X. Lu, M. Zhang, Y. Li and H. Yan, *Sci. China: Chem.*, 2020, **63**, 325–330.
- 50 X. Yang, B. Li, X. Zhang, S. Li, Q. Zhang, L. Yuan, D. Ko, W. Ma and J. Yuan, *Adv. Mater.*, 2023, **35**, 2301604.
- 51 J. Fu, H. Chen, P. Huang, Q. Yu, H. Tang, S. Chen, S. Jung, K. Sun, C. Yang, S. Lu, Z. Kan, Z. Xiao and G. Li, *Nano Energy*, 2021, **84**, 105862.
- 52 R. Yu, H. Yao, L. Hong, Y. Qin, J. Zhu, Y. Cui, S. Li and J. Hou, *Nat. Commun.*, 2018, **9**, 4645.
- 53 C. Yang, R. Yu, C. Liu, H. Li, S. Zhang and J. Hou, *ChemSusChem*, 2021, **14**, 3607–3613.
- 54 Y. Lee, D. Ho, F. Valentini, T. Earmme, A. Marrocchi, L. Vaccaro and C. Kim, *J. Mater. Chem. C*, 2021, **9**, 16506–16515.
- 55 R. Sun, J. Guo, Q. Wu, Z. Zhang, W. Yang, J. Guo, M. Shi, Y. Zhang, S. Kahmann, L. Ye, X. Jiao, M. A. Loi, Q. Shen, H. Ade, W. Tang, C. J. Brabec and J. Min, *Energy Environ. Sci.*, 2019, **12**, 3118–3132.
- 56 K. Jiang, J. Zhang, Z. Peng, F. Lin, S. Wu, Z. Li, Y. Chen, H. Yan, H. Ade, Z. Zhu and A. K.-Y. Jen, *Nat. Commun.*, 2021, **12**, 468.
- 57 J. Bertrandie, A. Sharma, N. Gasparini, D. R. Villalva, S. H. K. Paleti, N. Wehbe, J. Troughton and D. Baran, *ACS Appl. Energy Mater.*, 2022, **5**, 1023–1030.
- 58 X. Jiang, H. Kim, P. S. Deimel, W. Chen, W. Cao, D. Yang, S. Yin, R. Schaffrinna, F. Allegretti, J. V. Barth, M. Schwager, H. Tang, K. Wang, M. Schwartzkopf, S. V. Roth and P. Müller-Buschbaum, *J. Mater. Chem. A*, 2020, **8**, 23628–23636.
- 59 S. Grott, A. Kotobi, L. K. Reb, C. L. Weindl, R. Guo, S. Yin, K. S. Wienhold, W. Chen, T. Ameri, M. Schwartzkopf, S. V. Roth and P. Müller-Buschbaum, *Sol. RRL*, 2022, **6**, 2101084.
- 60 R. Yu, G. Wu, Y. Cui, X. Wei, L. Hong, T. Zhang, C. Zou, S. Hu, J. Hou and Z. Tan, *Small*, 2021, **17**, 2103497.
- 61 J. Qin, Q. Yang, J. Oh, S. Chen, G. O. Odunmbaku, N. A. N. Ouedraogo, C. Yang, K. Sun and S. Lu, *Adv. Sci.*, 2022, **9**, 2105347.
- 62 S. R. Cowan, A. Roy and A. J. Heeger, *Phys. Rev. B: Condens. Matter Mater. Phys.*, 2010, **82**, 245207.
- 63 R. Ma, Q. Fan, T. A. Dela Peña, B. Wu, H. Liu, Q. Wu, Q. Wei, J. Wu, X. Lu, M. Li, W. Ma and G. Li, *Adv. Mater.*, 2023, **35**, 2212275.
- 64 W. Gao, H. Fu, Y. Li, F. Lin, R. Sun, Z. Wu, X. Wu, C. Zhong, J. Min, J. Luo, H. Y. Woo, Z. Zhu and A. K.-Y. Jen, *Adv. Energy Mater.*, 2021, **11**, 2003177.
- 65 X. Liu, Z. Zhong, R. Zhu, J. Yu and G. Li, *Joule*, 2022, **6**, 1918–1930.
- 66 X. Liu, Z. Zhong, Y. Li, Z. Li, J. Zhou, R. Zhu, J. Yu and G. Li, *Adv. Energy Mater.*, 2023, **13**, 2301361.
- 67 H. F. Haneef, A. M. Zeidell and O. D. Jurchescu, *J. Mater. Chem. C*, 2020, **8**, 759–787.
- 68 Z. Gan, L. Wang, J. Cai, C. Guo, C. Chen, D. Li, Y. Fu, B. Zhou, Y. Sun, C. Liu, J. Zhou, D. Liu, W. Li and T. Wang, *Nat. Commun.*, 2023, **14**, 6297.
- 69 Y. Zhang, J. Wan, Y. Wang and Y. Ma, *RSC Adv.*, 2015, **5**, 97589–97597.